Optics Letters

Exploring the fundamental limits of integrated beam splitters with arbitrary phase via topology optimization

Abhishek Nanda,[1,2,3] Michael Kues,[1,2,4] and Antonio Calà Lesina[1,2,3,*]

[1]Hannover Centre for Optical Technologies, Leibniz University Hannover, Nienburger Str. 17, Hannover, 30167, Germany
[2]Cluster of Excellence PhoenixD, Leibniz University Hannover, Welfengarten 1A, Hannover, 30167, Germany
[3]Institute of Transport and Automation Technology, Leibniz University Hannover, An der Universität 2, Garbsen, 30823, Germany
[4]Institute of Photonics, Leibniz University Hannover, Nienburger Str. 17, Hannover, 30167, Germany
*antonio.calalesina@hot.uni-hannover.de

Received 16 November 2023; revised 22 January 2024; accepted 23 January 2024; posted 24 January 2024; published 20 February 2024

Optical beam splitters are essential for classical and quantum photonic on-chip systems. In integrated optical technology, a beam splitter can be implemented as a beam coupler with two input and two output ports. The output phases are constrained by the conservation of energy. In lossless beam splitters, the phase shift between the output fields is π and zero for excitation from the first and second input ports, respectively. Therefore, for excitation from both inputs, the phase between the output fields, defined as beam splitter phase (BSP), is π. The BSP leads to several phenomena, such as the quantum interference between two photons, known as the Hong–Ou–Mandel effect. By introducing losses, BSP values different than π become theoretically possible, but the design of 2×2 beam couplers with an arbitrary phase is elusive in integrated optics. Inspired by the growing interest on fundamental limits in electromagnetics and inverse design, here we explore the theoretical limits of symmetrical integrated beam splitters with an arbitrary BSP via adjoint-based topology optimization. Optimized 2D designs accounting for fabrication constraints are obtained for several combinations of loss and phase within the theoretical design space. Interestingly, the algorithm does not converge for objectives outside of the theoretical limits. Designs of beam splitters with arbitrary phase may find use in integrated optics for quantum information processing.

https://doi.org/10.1364/OL.512100

Introduction. Beam splitters are used to divide an input quantum state of single photons, atoms, or other quantum particles into numerous paths, which can then be recombined to produce interference patterns and create projection measurements to study various non-classical phenomena, like quantum entanglement. Interference between two or more photons is administered for quantum sensing [1] and metrology devices [2] and quantum information protocols, such as quantum teleportation, quantum key distribution, and quantum computation [3,4]. Specifically, linear optics quantum computation employs beam splitters along with phase shifters and photodetectors for the interaction between two photons via the Hong–Ou–Mandel (HOM) effect [5]. The phases at the output ports of a beam splitter affect the quantum interference between two photons. Conventional symmetrical beam splitters are lossless; the two output fields receive a relative phase flip for insertion at the first input and no relative phase flip for insertion at the second input. Hence, for both operation modes, the phase between the output fields, here referred to as the beam splitter phase (BSP), always plays out to be π. In frequency domain quantum interference, a HOM dip was observed when the BSP is π and a HOM peak appeared for BSP of 0 [6], which has no equivalence in conventional designs. In general, a specific phase adjustment is not possible in lossless beam splitters, and losses are required to enable phase adjustment within theoretical limits.

In integrated optical technology, beam splitters are implemented as 2×2 beam couplers (in this Letter, we treat beam splitter and beam coupler as synonyms), and have been used in integrated quantum logic gates, quantum information processing, and quantum computing [7]. However, integrated beam couplers with arbitrary phases are challenging to engineer with direct design techniques since only a few degrees of freedom for design are explored. Topology optimization is a powerful inverse design technique that minimizes or maximizes a target objective by (re-)distributing a given material in a design area [8]. Topology optimization can produce non-intuitive designs by addressing each pixel of the design space based on an efficient calculation of the gradient via the adjoint method [9]. Hence, it can provide integrated devices with the desired functionalities while maintaining a smaller footprint. In the realm of integrated optics, this method has been employed to design vortex beam emitters [10], single-photon sources [11], (de-)multiplexers [12,13], nonlinear optical components [14,15], high-power signal routers [16], mode and polarization splitters/converters [17], optical analog computing [18], and multi-layer grating couplers [19], also with the possibility of including foundry fabrication contraints [20,21]. Nevertheless, the use of this method in the field of integrated quantum technologies is in its nascent stage,

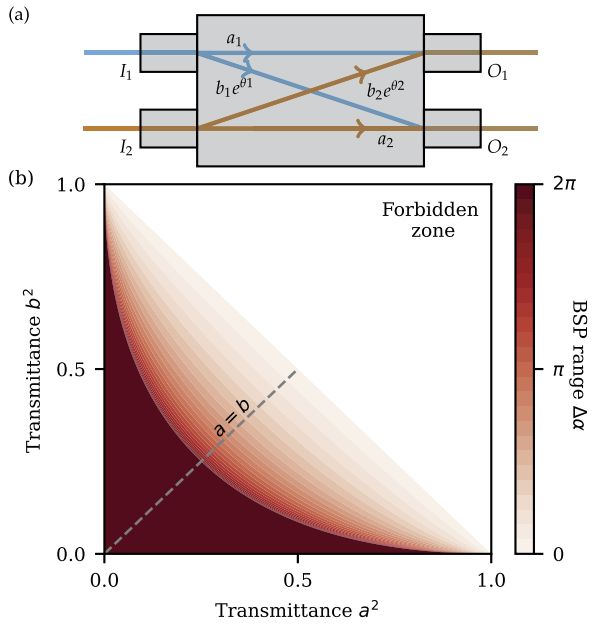

Fig. 1. (a) Schematic of a 2×2 integrated beam coupler and (b) phase range of the BSP (i.e., $\Delta\alpha$) for varying transmittances a^2 and b^2 [Eq. (3)].

with works on miniaturized optical quantum gates [22] and material platforms for quantum technologies [23].

In this Letter, we exploit topology optimization to inverse design symmetrical beam couplers with arbitrary loss–phase settings. While optimization for arbitrary phase was reported in 1×2 beam splitters [24], inverse design targeting arbitrary BSP in symmetrical 2×2 beam couplers is to date unreported. We demonstrate such designs for several combinations of loss–phase parameters within the theoretical limits while also satisfying typical fabrication constraints. There is a growing interest on physical limits in electromagnetism [25] and computational bounds for photonics inverse design [26]. In this context, lossy beam couplers with controllable phase are of broad interest [27] as they may expand the functionalities of integrated devices for quantum information processing and photonic quantum gates.

Fundamental limits of a beam splitter. The general scheme for a two-port integrated beam splitter in a linear implementation is shown in Fig. 1(a), where E_1 and E_2 are the electric fields associated with the beams at the input ports I_1 and I_2, respectively. Likewise, E_1' and E_2' are the electric fields associated with the beams at the output ports O_1 and O_2, respectively. The beam splitter matrix for this implementation is

$$\begin{bmatrix} E_1' \\ E_2' \end{bmatrix} = \begin{bmatrix} a_1 & b_2 e^{i\theta_2} \\ b_1 e^{i\theta_1} & a_2 \end{bmatrix} \begin{bmatrix} E_1 \\ E_2 \end{bmatrix}, \tag{1}$$

where a_1 and b_1 (a_2 and b_2) are the amplitudes of the transmission coefficients at the output ports for I_1 (I_2) port operation, and θ_1 (θ_2) is the phase shift between the transmission coefficients at the output ports for I_1 (I_2) port operation. Notice that a_1 and b_1 (a_2 and b_2) are real numbers and the phase information is entirely carried by θ_1 (θ_2). For a general solution to this set of equations, the beam splitter matrix does not need to be unitary, i.e., energy preserving. In a linear system, the output energy can never be greater than the input energy. Hence, simplifying Eq. (1) gives us the inequality

$$\left|a_1 E_1 + b_2 e^{i\theta_2} E_2\right|^2 + \left|a_2 E_2 + b_1 e^{i\theta_1} E_1\right|^2 \le |E_1|^2 + |E_2|^2 . \tag{2}$$

Here, the BSP can be defined as $\alpha = \theta_1 + \theta_2$. The condition of identical fields for photons gives $|E_1| = |E_2| = |E|$, and the symmetry of the two input operations yields $\theta_1 = \theta_2$, as well as $a_1 = a_2 = a$ and $b_1 = b_2 = b$. Therefore, Eq. (2) becomes

$$\left|\cos\frac{\alpha}{2}\right| \le \frac{(1 - a^2 - b^2)}{2ab}. \tag{3}$$

This means that the BSP α can assume values in the interval $[\pi - \Delta\alpha/2, \pi + \Delta\alpha/2]$, where the phase range $\Delta\alpha$ depends on a^2 and b^2, i.e., the losses in the system. This inequality relation is plotted in Fig. 1(b) for different values of a^2 and b^2, where the strength of the color represents the value of $\Delta\alpha$.

The BSP α affects the quantum interference between two photons. Conventional lossless beam couplers do not allow the variation of α, because no loss signifies $a^2 + b^2 = 1$, which leads to a BSP $\alpha = \pi$ [see Fig. 1(b)]. Hence, it becomes necessary to introduce losses to achieve arbitrary phase values in agreement with Eq. (3). In general, both balanced (i.e., $a = b$) and unbalanced (i.e., $a \neq b$) beam couplers can be designed with precise phase adjustment. Nevertheless, for many quantum applications, the output ports need to be equiprobable ($a = b$); see dotted gray line in Fig. 1(b). Hence, the focus of this research is on balanced symmetrical lossy beam splitters. The loss–phase relation for these beam couplers can be derived from Eq. (3) as

$$\left|\cos\frac{\alpha}{2}\right| \le \frac{2d^2}{1 - 2d^2}, \tag{4}$$

where $d^2 = (1 - 2a^2)/2$ is the intensity loss in each path for a symmetrical beam splitter. For $d^2 = 0$, we have $\Delta\alpha = 0$. By increasing d^2, the range of permitted phase values $\Delta\alpha$ increases, reaching the maximum value $\Delta\alpha = 2\pi$ for $d^2 = 0.25$.

Inverse design method. In order to simulate, design, and optimize an integrated beam splitter with arbitrary phase based on the theoretical limits in Eq. (4), we employed the open-source software package Meep [28]. This solver implements the finite-difference time-domain (FDTD) method [29] and includes a hybrid time/frequency domain adjoint solver [30] where the gradients are calculated via automatic differentiation through the open-source package Autograd [31]. We performed the 2D inverse design of 2×2 beam couplers made of Si ($n = 3.4$) and embedded in SiO_2 ($n = 1.44$). The operating wavelength is 1.55 μm. The design domain was optimized to achieve devices with a small footprint, resulting in a design area of 3×1.6 μm^2. The space step of the FDTD simulation, which coincides with the pixel size of the optimization, is 25 nm. The waveguide ports on the two sides of the beam coupler have 300 nm thickness and are 300 nm apart (edge-to-edge). The fundamental mode is injected at each input port. Field monitors are used at the output ports to perform a mode decomposition, such that the objective function always acts on the fundamental mode.

The optimization algorithm is illustrated in Fig. S1 (Supplement 1) as a flow chart. A design variable ρ_i called density is associated with each pixel in the design domain and must be optimized. The density ρ_i assigns a permittivity ε_{opt} to each pixel between the dielectric permittivities of Si (ε_{Si}) and SiO_2 (ε_{SiO_2}) based on the linear mapping scheme $\varepsilon_{opt}(\rho_i) = \varepsilon_{SiO_2} + \rho_i\left(\varepsilon_{Si} - \varepsilon_{SiO_2}\right)$. The optimization starts with all pixels in the design domain being assigned $\rho_i = 0.5$. At each

iteration, two FDTD simulations (forward and adjoint) are performed to evaluate the gradient of the objective with respect to the design variables ρ_i, and the gradient is then used to update the design variables following operations of filtering and projection [32]. The optimization includes a binarization hyperparameter increased each time an optimization cycle converged to a solution. This was used to gradually reduce any intermediate permittivity values in the design domain and achieve a binary physical design with permittivity values of only Si and SiO_2, i.e., $\rho_i = 1$ or $\rho_i = 0$, respectively. Additionally, the optimization routine establishes symmetry conditions and accounts for manufacturability constraints. The manufacturability constraints for this work represents a nonlinear conic filter with minimum feature size of 100 nm, which is a typical feature size achievable by modern manufacturing techniques.

This work incorporates multiple objective functions, i.e., output loss per path (d^2) and BSP (α), via an epigraph formulation of the optimization process. These target functions and their combination need to be automatic differentiable. This necessitated the formulation of a weighted phase function (f_{BSP}), which was then combined with the intensity objective (f_{int}). The multi-objective optimization problem can be formulated as

$$\min_{\rho_i, E_1, E_2} \operatorname{epi}\left(f_{int} + f_{BSP}\right), \tag{5}$$

where

$$f_{d^2} = \left|0.5 - d^2 - a_1^2\right| + \left|0.5 - d^2 - b_1^2\right| + \left|0.5 - d^2 - a_2^2\right| + \left|0.5 - d^2 - b_2^2\right|$$

and

$$f_{BSP} \equiv |\alpha/2 - \theta_1| + |\alpha/2 - \theta_2| \pmod{2\pi}$$

subject to

$$\nabla \times \nabla \times \mathbf{E}_1 - \omega^2 \mu \varepsilon_{opt}(\rho_i)\mathbf{E}_1 = -i\omega\mu\mathbf{J}_1$$
$$\nabla \times \nabla \times \mathbf{E}_2 - \omega^2 \mu \varepsilon_{opt}(\rho_i)\mathbf{E}_2 = -i\omega\mu\mathbf{J}_2,$$

where $\mathbf{E}_1$ ($\mathbf{E}_2$) is the complex electric field, $\mathbf{J}_1$ ($\mathbf{J}_2$) is the current source density, a_1^2 and b_1^2 (a_2^2 and b_2^2) are the transmittances, and θ_1 (θ_2) is the output phase difference associated with input port I_1 (I_2) excitation, respectively. Here the magnetic permeability μ and frequency ω are constant.

Results and discussion. Symmetrical beam splitters were optimized for several loss–phase combinations, and the results of the optimization are summarized in Fig. 2, where red crosses and blue dots show the design targets and performance of optimized designs, respectively. The analytical limits in Eq. (4) are represented as dotted gray lines in Fig. 2, which visually show the increase of $\Delta\alpha$ for increasing losses with a funnel-like shape. Convergence is achieved for values of loss and phase within the theoretical limits, while for design targets outside such limits, the optimizations fail to converge. In a few cases, blue dots and red crosses do not overlap, thus showing a deviation of the performance of the optimized design from the target response, which is here quantified through the mean of linear deviation $\mathrm{MLD}(d^2, \alpha) = \Sigma\sqrt{(d_{opt}^2 - d_{tar}^2)^2 + (\alpha_{opt} - \alpha_{tar})^2}/N$, where the sum is performed over the number of designs N. For increasing losses (see three regions defined for convenience in Fig. 2), the MLD decreases, being 1.16%, 0.53%, and 0.34%, in the low loss, medium loss, and high loss regions, respectively.

Three optimized designs A, B, and C are selected for each region in Fig. 2 and discussed in detail in Fig. 3. The first structure (Design A) was obtained in the region of low loss and

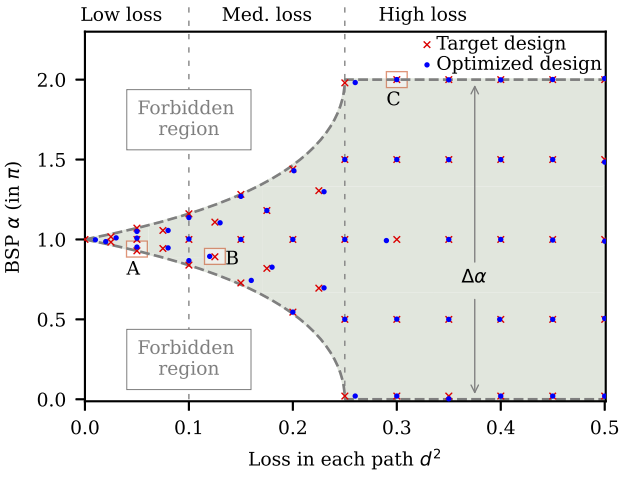

Fig. 2. Optimization results for beam couplers with arbitrary phase: achieved BSP (α) for increasing loss in each port (d^2).

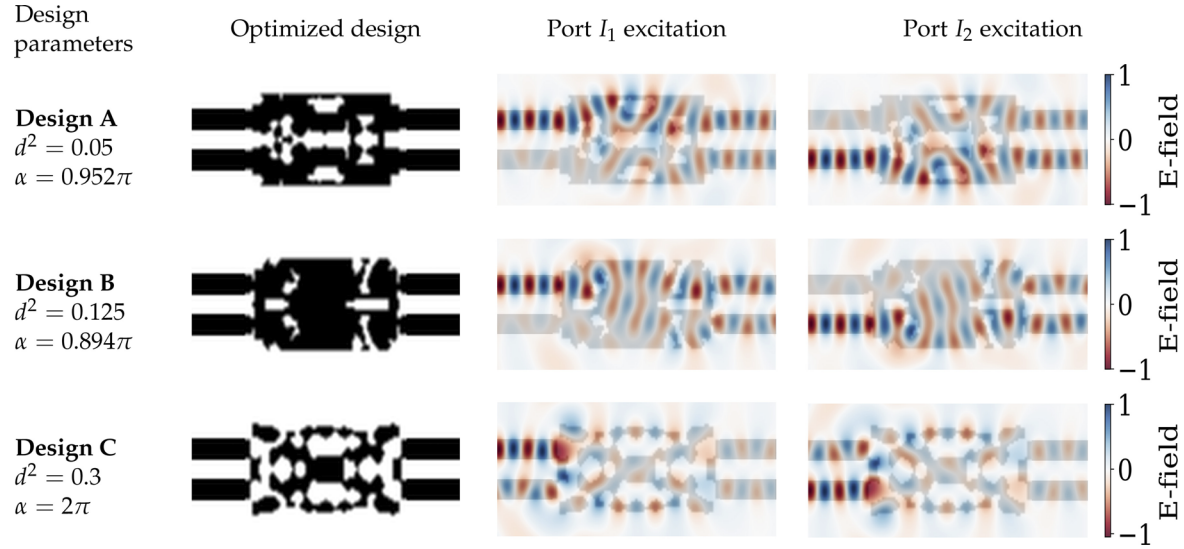

Fig. 3. Selection of the three topology optimized designs (A, B, and C from Fig. 2) and electric field distributions for excitation from port I_1 or I_2.

low phase tunability, i.e., loss $d^2 = 5\%$ at each port with BSP $\alpha = 0.952\pi$. The second structure (Design B) falls in the medium loss range, with a loss $d^2 = 12.5\%$ at each port and a BSP $\alpha = 0.894\pi$. The last structure (Design C) was optimized in the high loss regime where large phase tunability can be achieved, i.e., loss $d^2 = 30\%$ at each port with BSP $\alpha = 2\pi$. In Fig. 3, we also show the distribution of the out-of-plane electric field component (real part) at the wavelength of 1.55 μm for excitation from ports 1 and 2. We observe the higher scattering losses in Design C, along with the lower total fields at the output ports. We note that the phase front at the output port looks distorted, but the optimization was performed targeting the fundamental mode of interest. The designs reported in Fig. 2 are made available as binary files in Dataset 1, Ref. [33]. These binary files can be reintroduced into Meep and the device performances validated via FDTD simulations.

Although we used 2D inverse design as a proof of principle, in practice 3D designs are needed. For further validation, our 2D designs were analyzed with 3D FDTD simulations by extruding the design in the third dimension with a finite thickness. As expected, the deviation between 2D and 3D simulations in terms of total losses decreases for increasing thickness of the device. However, the splitting ratio as a function of thickness cannot be predicted and deviation from the desired case can be significant. Hence, in order to bring such concept to an experimental scenario, 3D optimization is required, with the associated increase of computational cost and optimization time. The provided 2D designs could be used as an initial guess for 3D optimization.

We have demonstrated that beam splitters with arbitrary phase can be designed via topology optimization within the theoretical limits. Any design target outside of the analytical limit (in the forbidden region) did not converge to the objectives. Although we have focused on balanced symmetrical beam splitters, this design method can be extended to unbalanced symmetrical beam splitters, e.g., $a = 2b$ or any other ratio based on specific applications. As the Hong–Ou–Mandel effect depends on the phase α, we believe novel functionalities can emerge for different phase values, and we hope the proposed non-intuitive designs with arbitrary phase will motivate novel experiments in quantum information processing.

Funding. European Research Council (QFreC project, Grant agreement ID 947603); Deutsche Forschungsgemeinschaft (EXC 2122, Project ID 390833453).

Acknowledgment. Simulations were performed, in part, on the central computing cluster operated by Leibniz University IT Services (LUIS), which is funded by the Deutsche Forschungsgemeinschaft (DFG, German Research Foundation), project number INST 187/742-1 FUGG. We also acknowledge the computing time granted by the Resource Allocation Board and provided on the supercomputer Lise and Emmy at NHR@ZIB and NHR@Göttingen as part of the NHR infrastructure (calculations were conducted with computing resources under the project nip00059).

Disclosures. The authors declare no conflicts of interest.

Data availability. Data underlying the results presented in this paper are available in Dataset 1, Ref. [33].

Supplemental document. See Supplement 1 for supporting content.

REFERENCES

1. C. Degen, F. Reinhard, and P. Cappellaro, Rev. Mod. Phys. **89**, 035002 (2017).
2. V. Giovannetti, S. Lloyd, and L. Maccone, Nat. Photonics **5**, 222 (2011).
3. S. Slussarenko and G. J. Pryde, Appl. Phys. Rev. **6**, 041303 (2019).
4. W. Luo, L. Cao, Y. Shi, *et al.*, Light: Sci. Appl. **12**, 175 (2023).
5. E. Knill, R. Laflamme, and G. J. Milburn, Nature **409**, 46 (2001).
6. A. K. Kashi and M. Kues, Laser Photonics Rev. **15**, 2000464 (2021).
7. W. Wang, Y. Xu, and Z. Chai, Adv. Photonics Res. **3**, 2200153 (2022).
8. J. Jensen and O. Sigmund, Laser Photonics Rev. **5**, 308 (2011).
9. C. M. Lalau-Keraly, S. Bhargava, O. D. Miller, *et al.*, Opt. Express **21**, 21693 (2013).
10. A. D. White, L. Su, D. I. Shahar, *et al.*, ACS Photonics **10**, 803 (2022).
11. O. Yesilyurt, Z. A. Kudyshev, A. Boltasseva, *et al.*, ACS Photonics **8**, 3061 (2021).
12. A. Piggott, J. Lu, K. G. Lagoudakis, *et al.*, Nat. Photonics **9**, 374 (2015).
13. L. F. Frellsen, Y. Ding, O. Sigmund, *et al.*, Opt. Express **24**, 16866 (2016).
14. T. W. Hughes, M. Minkov, I. A. D. Williamson, *et al.*, ACS Photonics **5**, 4781 (2018).
15. Z. Lin, X. Liang, M. Lončar, *et al.*, Optica **3**, 233 (2016).
16. J. B. Slaby, A. M. Hammond, and S. E. Ralph, in *CLEO 2023*, (Optica Publishing Group 2023), paper STh4G.4.
17. J. Lu and J. Vučković, Opt. Express **21**, 13351 (2013).
18. V. Nikkhah, M. J. Mencagli, and N. Engheta, Nanophotonics **12**, 3019 (2023).
19. A. M. Hammond, J. B. Slaby, M. J. Probst, *et al.*, Opt. Express **30**, 31058 (2022).
20. A. Y. Piggott, E. Y. Ma, L. Su, *et al.*, ACS Photonics **7**, 569 (2020).
21. M. F. Schubert, A. K. C. Cheung, I. A. D. Williamson, *et al.*, ACS Photonics **9**, 2327 (2022).
22. L. He, D. Liu, J. Gao, *et al.*, Sci. Adv. **9**, eadg6685 (2023).
23. C. Shang, J. Yang, A. M. Hammond, *et al.*, ACS Photonics **10**, 1019 (2023).
24. A. M. Hammond, J. B. Slaby, M. J. Probst, *et al.*, ACS Photonics **10**, 808 (2022).
25. P. Chao, B. Strekha, R. Kuate Defo, *et al.*, Nat. Rev. Phys. **4**, 543 (2022).
26. G. Angeris, J. Vuckovic, and S. P. Boyd, ACS Photonics **6**, 1232 (2019).
27. R. Uppu, T. A. W. Wolterink, T. B. H. Tentrup, *et al.*, Opt. Express **24**, 16440 (2016).
28. A. F. Oskooi, D. Roundy, M. Ibanescu, *et al.*, Comput. Phys. Commun. **181**, 687 (2010).
29. A. Taflove and S. C. Hagness, *Computational Electrodynamics: The Finite-Difference Time-Domain Method*, 3rd ed. (Artech House, 2005).
30. A. M. Hammond, A. Oskooi, M. Chen, *et al.*, Opt. Express **30**, 4467 (2022).
31. D. Maclaurin, D. Duvenaud, and R. P. Adams, in *ICML 2015 AutoML Workshop* (2015), p. 5.
32. B. S. Lazarov, F. Wang, and O. Sigmund, Arch. Appl. Mech. **86**, 189 (2016).
33. A. Nanda, M. Kues, and A. Calà Lesina, "Topology optimized 2D beam splitters with various loss-phase targets," figshare (2023). https://doi.org/10.6084/m9.figshare.24570241.